Macroscopic Electro Thermal Simulation of Contact Resistances

Bachelor's Thesis

Presented by:
Müller, Philipp Thomas

Prof. Dr. Manuel Torrilhon
Dr. Jörg Ostrowski

This work was submitted to the RWTH - Center for Computational Engineering Science - Mathematics Division

Aachen, January 26, 2016

Contents

List of Figures

List of Tables

1 Introduction

Power devices developed by ABB such as high voltage switchgear rely on an exact prediction of their current density distribution and the resulting heat generation. Unexpectedly high losses may lead to an overheating and, hence, a failure of the device. An important additional resistance results from electrical contacts. These impose a resistance to the device, which is hard to estimate and may change during the device's lifespan. Important to note is that no contact type eliminates the contact resistance completely. The overheating can, for example, in circuit breakers, result in a failure. Hence, a determination of the contact resistances and their impact on the device's current density and temperature distribution is essential for avoiding malfunctions. In this field simulations have become popular for minimizing the need of cost intensive experiments and for enhancing the understanding of local effects.

Researches in this field started with experiments conducted by Ragnar Holm, whose results are collected in his book "*Electrical Contacts*". It presents rough estimation formulas for the contact resistance and the current flow close to electrical contacts. Recent simulations focus on simulating the contact resistances on a microscopic scale by approximating the surface topography mathematically. One exemplary approach is presented in the paper "*Conductance of rough random profiles*", written by M. Ciavarella et al., who describe the surface profile by Weierstrass series with random phases.

In this thesis, however, the current distribution is simulated on a macroscopic scale under neglecting the microscopic contact surface topography. Hereby, the aim is the determination of the current density and heat distribution for devices comprising contact resistances. For simulating the current density distribution, we extend a *C++* tool called HADAPT, which is a finite elements method (FEM) simulation tool developed by the industrial partner ABB Switzerland AG for internal usage. Before HADAPT was extended, it solved Maxwell's equations in a robust formulation yielding stable solutions for all frequencies; however, neglecting the impact of possibly occurring contact resistances. In the course of this thesis, HADAPT is extended in order to be capable of solving Maxwell's equations for devices comprising contact resistances. The current distribution yields an ohmic loss distribution, which results, for example, from wire resistances, and contact resistances. For simulating the heat distribution, this ohmic loss distribution is exported from HADAPT and imported into the commercial fluid dynamics solver Fluent. In this solver the heat generation, as well as the heat transfer due to temperature gradients, are simulated.

2 Physics of Contact Resistances

Electric contact resistances occur between solids in contact and consists of

- constriction resistances due to microscopically rough surfaces,
- film resistances due to thin layers from for example oxidations,
- and transition resistances due to discontinuities in the crystal structure.

These resistances are discussed in the following sections in descending order of influence.

2.1 Constriction Resistance

The constriction resistance is unavoidable for solid conductors in contact. Since every solid surface is microscopically rough with randomly distributed asperities of varying heights, two conductors are only in contact at a few points [12]. These contact points are hereinafter referred to as *a-spots*. They limit the conducting area and constrict the current paths to pass through them, as shown in Figure 1. This results in a constriction resistance, whose magnitude depends for a contact on the a-spots' magnitude, area, and shape.

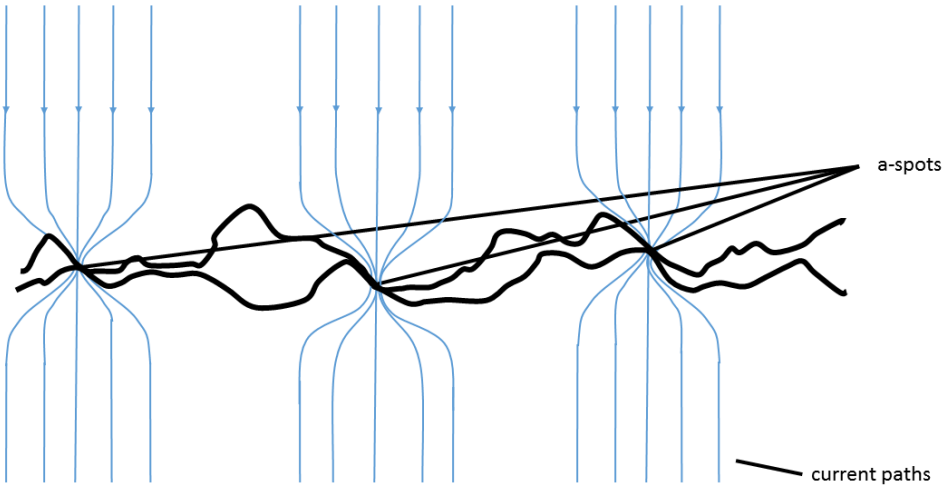

Figure 1: A schematic visualization of distorted current paths through a-spots [23]

The real contact area A_c is formed by the union of all a-spots' areas, whereas the nominal contact area A_n denotes the macroscopic area of contact. A_c can be increased for materials with finite hardness by plastic and elastic deformations

through an applied mechanical force F, which enlarges the number of a-spots and their area. A_c can be approximated as

$$A_c = \frac{F}{\xi H}, \tag{1}$$

where F in N denotes the force component normal to the contact and H the material's hardness in Pa. The hardness only depends on the material's yield stress. ξ, the pressure factor, is equal to 1 in most practical contact systems even though it depends on the surface topography and the contact materials. It is neglected in the following. [3]

Equation (1) shows that A_c is not a function of A_n, which, at first, is not intuitive. The reason for this becomes apparent for an exemplary setup. In this there are two contacts, one small contact s and one large contact l, having the macroscopic contact areas A_{n_s} and A_{n_l}, respectively. Both contacts are assumed to be similar regarding their surface asperities, however, A_{n_l} is ten times larger than A_{n_s}. Thus, the contact area for contact l, A_{c_l}, comprises ten times more a-spots than A_{c_s}. An applied force F is, accordingly, distributed in A_{n_s} on only n a-spots, whereas it is distributed on $10n$ a-spots in A_{n_l}. Under the assumption of a fully plastic deformation, F deforms each a-spot on average to an a-spot radius a in the contact s and $a/\sqrt{10}$ in the contact l [23]. This leads to the contact areas being expressed by

$$A_{c_s} = n\pi a^2 = 10n\pi\frac{a^2}{10} = A_{c_l},$$

which implies A_{c_s} and A_{c_l} being equal. [23]

An estimation for the constriction resistance R_s is derived in the following exemplarily for a single circular a-spot between two semi-infinite cylinders, as shown in Figure 2, and extended for a more general application. However, it is still limited to isotropic topographies and circular a-spots, which can be assumed in general, except for surfaces having "roughness[es with] a directional characteristic, [as] e.g., rolled-metal sheets" [3].

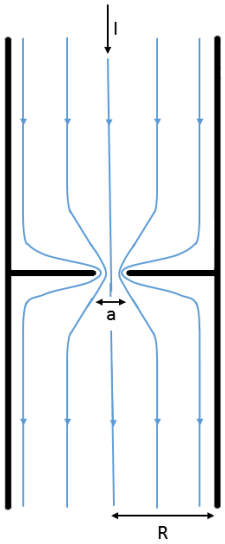

Figure 2: An exemplary circular a-spot between two semi infinite cylinders in contact [22]

Assuming the current path through the a-spot is not influenced by inductive effects and current sources, the current conservation law

$$\operatorname{div} \mathbf{j} = 0$$

holds. Hereby, $\mathbf{j}$ denotes the current density in $\mathrm{A/m^2}$ with

$$\mathbf{j} = -\frac{1}{\rho}\mathbf{grad}\phi,$$

where ϕ denotes the electric potential in V and ρ the resistivity in $\frac{\Omega}{\mathrm{m}}$. Also assuming a constant resistivity $\rho = const$ close to the a-spot leads to

$$\Delta\phi = 0. \tag{2}$$

The constriction resistance R_s then follows from (2), a partial differential equation (PDE), as

$$R_s = \frac{\rho}{2a}\left[1 - 1.41581(\frac{a}{R}) + 0.06322(\frac{a}{R})^2 + 0.15261(\frac{a}{R})^3\right]$$

with the a-spot radius $a/2$ and the cylinder radius R, see Figure 2, and simplifies for $\frac{a}{R} \ll 1$ to

$$R_s = \frac{\rho}{2a}. \tag{3}$$

Due to the assumptions stated above, Equation (3) is only valid for a single circular a-spot with $\frac{a}{R} \ll 1$. The steps for deriving this equation can be found in detail in the paper "The potential distribution in a constricted cylinder" [22].

Equation (3) is extended by Greenwood in [8] for contacts with two different contact materials. For the resistivities ρ_1 and ρ_2, his estimation can be expressed as

$$R_s = \frac{\rho_1 + \rho_2}{4}\sqrt{\frac{\pi}{F}\eta H},$$

[23]. η is hereby an empirical constant close to unity depending on the contact type and the hardness H of the softer material. This shows that the contact resistance is proportional to $\sqrt{F^{-1}}$ for a given contact and therefore decreases for an increasing mechanical force.

2.2 Film resistance

The film resistance is caused by additional layers on the conductor surfaces, which enlarge the resistivity ρ. Since we only consider stationary contacts, most film resistance effects are not discussed here. Stationary contacts are, in contrast to moving contacts, most of the time in contact leading to prevention of mechanical wear and films. In spite of that, the most common films, which result either from physical or chemical absorption, are discussed the following sections.

2.2.1 Physical Adsorption

Physical absorption leads to a bond between the contact surface and adsorbate due to e.g., van der Waals forces. Van der Waals forces arise from temporary displacements of electrons in the electron cloud of atoms. These atoms become temporary dipoles and in turn induce corresponding dipole atoms. These attract each other by the resulting electrostatic dipole force - the van der Waals force [24]. The resulting bond energies are low ($20kJ/mol$) and can be easily ruptured by applied mechanical forces on the contacts [3]. An additional so called tunnel resistance σ is seen in experiments with noble gas atoms as adsorbate leading to the film resistance R_f for a single circular a-spot expressed as

$$R_f = \frac{\rho}{2a} + \frac{\sigma}{\pi a^2}.$$

σ is in the order of $10^{-}13\,\Omega\mathrm{m}^2$ [12] and therefore physical absorption can be neglected in most applications.

2.2.2 Chemical Adsorption

In contrast to the physical adsorption, layers formed by chemical absorption, for example by oxidations and fretting, have high bond energies (about $80 - 400\,\mathrm{kJ/mol}$ [3]) and can, therefore, not easily be ruptured. In the following I discuss the chemical adsorption of oxygen by metal surfaces at room temperature. Oxygen molecules often are physical adsorbed at first, but are separated into their atoms and chemically adsorbed in fractions of a seconds [12]. This leads to a very thin layer of atoms, often referred to as monolayer. It results within seconds even for an oxygen pressure of $0.013\,332\,2\,\mathrm{Pa}$ [12], whereas the atmospheric oxygen pressure is already $79\,113.493\,\mathrm{Pa}$. These layers grow as adsorbed atoms become part of the metal's lattice and metal ions migrate through the layer to the outside. Therefore, additional atoms can be chemically adsorbed by the migrated metal ions. This effect only occurs if the bond energy between the contact material and the adsorbate is higher than between the proceeding adsorbate molecule and the metal. This leads to practically no growth for the combination of gold and oxygen, but a comparably well growth for the combination of copper and oxygen. [12]

The chemical adsorbed films can be passed by electrons by the tunnel effect resulting in a tunnel resistance. The tunnel effect is a quantum mechanical phenomenon allowing particles to pass potential barriers (resistances) even though their energies, according to classical theories, are too low. The tunnel resistance is the resulting from this effect [24]. A thick visible film of adsorbate layers is regarded as insulating and constricts the current paths to ruptured areas. These films manly only establish at moderate temperature, where the necessary activation energies for the oxidation are given.[12]

2.3 Transition Resistance

The electric current flow can be described as an unorganized flow through the crystal structure of the materials. As the crystal structure changes discontinuously at the area of contact, electrons could be reflected partly. Through experiments conducted by Holm [13], these resistances are estimated to be in the order of the grain boundary resistance, which are the interfaces between

crystals [12] and present throughout the whole conductor. Hence, they can be generally neglected.

2.4 Summary

To sum up, the contact resistance can be split into a constriction R_s, a film resistance R_f and a transition part.

- The surface topography of contact interfaces and therefore the constriction resistance depends on many unpredictable factors, but represents the governing resistance for stationary contacts.
- The film resistance depends heavily on the environment the contact is placed in. Environments with a high potential for oxidations lead to thicker layers of adsorbates and, hence, to a high film resistance. For stationary contacts at room temperature, mostly monolayers occur and can therefore be neglected.
- The transition resistance has proven to have no impact at all.

Therefore, the commonly employed well spread estimation equation for the contact resistance can be expressed as

$$R_s = \frac{\rho_1 + \rho_2}{4} \sqrt{\frac{\pi}{F} \eta H}. \tag{4}$$

Due to the random surface topography and the empirical constant η it is typically not possible to estimate the contact resistance reliably for an arbitrary contact. An exception is a simulation series of similar contacts. Therefore, a measured contact resistance value is required in the following as user input. In spite of that, (4) gives a possibility to extend the electro-thermal simulation to an electro-thermal-mechanical simulation.

3 Modeling

In this chapter the simulation models for the electromagnetic and fluid dynamics simulation are discussed. The electromagnetic simulation model is derived from Maxwell's equations in a stabilized formulation, which was introduced in [11]. This stabilized formulation is derived and reformulated into a variational formulation in sections 3.1.1 - 3.1.4. It is extended in section 3.2 in order to include contact resistances. The extended system is solved in section 3.3 by employing a finite elements method (FEM). The fluid dynamics model covers convection, radiation and conduction effects, and is presented in section 3.4.

3.1 Robust Formulation of Maxwell's Equations

3.1.1 $\mathbf{a}\varphi$ - Formalism

Maxwell's equations describe electromagnetic fields including their interaction. For time dependent fields and arbitrary materials, they are given by

$$\begin{aligned} \operatorname{div} \mathbf{b}(\mathbf{x},t) &= 0, \\ \mathbf{curl}\, \mathbf{e}(\mathbf{x},t) + \frac{\partial \mathbf{b}(\mathbf{x},t)}{\partial t} &= 0, \\ \operatorname{div} \mathbf{d}(\mathbf{x},t) &= \rho(\mathbf{x},t), \\ \mathbf{curl}\, \mathbf{h}(\mathbf{x},t) - \frac{\partial \mathbf{d}(\mathbf{x},t)}{\partial t} &= \mathbf{j}(\mathbf{x},t), \\ \mathbf{d} &= \epsilon \mathbf{e}, \\ \mathbf{b} &= \mu \mathbf{h}, \end{aligned} \tag{5}$$

where $\mathbf{b}$ denotes the magnetic field, $\mathbf{e}$ the electric field, ρ the charge density, and $\mathbf{j}$ the current density [16]. ϵ and μ are the material depending constants electric permittivity and magnetic permeability, respectively. By introducing a scalar potential φ and a vector potential $\mathbf{a}$ as

$$\begin{aligned} \mathbf{b} &= \mathbf{curl}\, \mathbf{a}, \\ \mathbf{e} &= -\nabla\varphi - \dot{\mathbf{a}}, \end{aligned}$$

the system (5) consisting of four first-order partial differential equations (PDEs) reduces to two second-order PDEs. The new system can by expressed by using the Coulomb gauged $\mathbf{a}\varphi$ - formalism as

$$\begin{aligned} \mathbf{curl}\,\frac{1}{\mu(\mathbf{x})}\,\mathbf{curl}\,\mathbf{a}(\mathbf{x},t) + \epsilon\,\mathbf{grad}\,\frac{\partial\varphi(\mathbf{x},t)}{\partial t} + \epsilon\frac{\partial^2\mathbf{a}(\mathbf{x},t)}{\partial t^2} &= \mathbf{j}(\mathbf{x},t), \\ \operatorname{div}\epsilon\mathbf{a}(\mathbf{x},t) &= 0. \end{aligned} \tag{6}$$

Further information including background regarding the choice of $\mathbf{a}$ and φ can be found in [16].

3.1.2 Transformation to the Frequency Domain

Circuits with oscillating excitations of an angular frequency ω lead to electromagnetic fields operating at ω; after a finite calibration time, they can be regarded as time harmonic fields [6]. Thus $\mathbf{a}(\mathbf{x},t)$ can be split into a spatial part $\hat{\mathbf{a}}(\mathbf{x})$ and a transient part $\exp(i\omega t)$. With the trial

$$\mathbf{a}(\mathbf{x},t) = \operatorname{Re}\{\hat{\mathbf{a}}(\mathbf{x})\exp(i\omega t)\}$$

applied to all field variables, Maxwell's equations in (6) become

$$\begin{aligned} \operatorname{Re}\{[\mathbf{curl}\,\frac{1}{\mu(\mathbf{x})}\,\mathbf{curl}\,\hat{\mathbf{a}}(\mathbf{x}) + \epsilon i\omega\,\mathbf{grad}\,\hat{\varphi}(\mathbf{x}) - \\ \epsilon\omega^2\hat{\mathbf{a}}(\mathbf{x})]\cdot\exp(i\omega t)\} = \operatorname{Re}\{[\hat{\mathbf{j}}(\mathbf{x})]\cdot\exp(i\omega t)\}, \end{aligned} \tag{7a}$$

$$\operatorname{Re}\{[\operatorname{div}\epsilon\hat{\mathbf{a}}(\mathbf{x})]\cdot\exp(i\omega t)\} = 0. \tag{7b}$$

As (7a) and (7b) have to be valid for all t, they can be reduced to

$$\begin{aligned} \mathbf{curl}\,\frac{1}{\mu(\mathbf{x})}\,\mathbf{curl}\,\hat{\mathbf{a}}(\mathbf{x}) + \epsilon i\omega\,\mathbf{grad}\,\hat{\varphi}(\mathbf{x}) - \epsilon\omega^2\hat{\mathbf{a}}(\mathbf{x}) &= \hat{\mathbf{j}}(\mathbf{x}), \\ \operatorname{div}\epsilon\hat{\mathbf{a}}(\mathbf{x})\} &= 0. \end{aligned} \tag{8}$$

By using Ohm's law $\mathbf{j} = \sigma\mathbf{E} = -(\sigma\,\mathbf{grad}\,\hat{\varphi} + i\sigma\omega)$, Maxwell's equations in (8) can be expressed as

$$\begin{aligned} \mathbf{curl}\,\frac{1}{\mu(\mathbf{x})}\,\mathbf{curl}\,\hat{\mathbf{a}} + \epsilon i\omega\,\mathbf{grad}\,\partial\hat{\varphi} - \epsilon\omega^2\hat{\mathbf{a}} &= -\left(\sigma\,\mathbf{grad}\,\hat{\varphi} + i\sigma\omega\hat{\mathbf{a}}\right) \\ \operatorname{div}\epsilon\hat{\mathbf{a}}(\mathbf{x}) &= 0. \end{aligned} \tag{9}$$

It can be seen that Maxwell's equations in (9) do not depend on t anymore; their solution only depends on the angular frequency ω in the frequency domain. For simplicity the hat $\hat{}$ denoting the spatial terms is omitted in the following.

3.1.3 Variational Formulation

For applying the FEM, the system (9) needs to be reformulated into a variational formulation. The following brief introduction to variational formulations is based on [19], where further information can be found. The reformulation is shown at first exemplarily in a simplified manner and, at the end, is applied to (9).

For this, we consider Poisson's equation in one dimension: find $u \in \mathrm{C}^2(\bar{\Omega}) \cap \mathrm{C}^0(\Omega)$ such that

$$\begin{aligned} -\Delta u(x) &= f(x) \quad x \in \bar{\Omega}, \\ u(x) &= 0 \quad x \in \partial\Omega. \end{aligned} \tag{10}$$

Hereinafter, Ω denotes the domain, $\bar{\Omega}$ the domain excluding the boundary and $\partial\Omega$ solely the domain's boundary. Multiplying (10) by an arbitrary function $u' \in \mathrm{C}_0^1(\bar{\Omega})$ and integrating it over Ω leads to

$$\int_\Omega \Delta u u' \,\mathrm{d}x = \int_\Omega f u' \,\mathrm{d}x. \tag{11}$$

Applying Green's first identity to (11) yields

$$\int_\Omega \nabla u \nabla u' \,\mathrm{d}x - \cancelto{0}{\int_{\partial\Omega} (\nabla u \cdot n) u' \,\mathrm{d}x} = \int_\Omega f u' \,\mathrm{d}x. \tag{12}$$

Equation (12) is hereby the variational formulation with n denoting the outer normal. Functions similar to $u' \in C_0^1(\bar{\Omega})$ are hereinafter referred to as test functions.

The advantage of (12) in contrast to (10) is that the formulation (12) is less demanding regarding the continuity of u. In (12) u only needs to be an element of $\mathrm{C}^1(\bar{\Omega}) \cap \mathrm{C}^0(\Omega)$, whereas it needs to be an element of $\mathrm{C}^2(\bar{\Omega}) \cap \mathrm{C}^0(\Omega)$ in (10). This, however, implies that the solution u for (12) does not necessarily solve (10) point-wise. The variational solution u solves (10) point-wise only if $u \in \mathrm{C}^2(\bar{\Omega}) \cap \mathrm{C}^0(\Omega)$. For a mathematical correct variational formulation, a complete space - the sobolev space - is used. The sobolev space $H_0^1(\Omega)$ comprises all on Ω Lebesgue square integrable functions, which disappear on the boundary and whose weak first partial differentiation is still square integrable.

The reformulation to variational formulations is applied to Maxwell's equations in (9) by relying on the test function spaces

$$V := \left\{ \mathbf{v} \in \mathbf{H}(\mathbf{curl}, \Omega) : \mathbf{curl}_\Gamma \, \mathbf{v_t} = 0 \, \text{on} \, \partial\Omega, \int_\tau \mathbf{v} \cdot \mathrm{d}s = 0 \right\},$$
$$H(U) := \left\{ \psi \in H^1(\Omega) : \psi_{\Gamma_0} = 0, \psi_{\Gamma_1} = U \right\},$$

which are introduced in [11] along with presupposed boundary conditions. U denotes the applied voltage excitation value. The variational formulation follows as: seek $\mathbf{a} \in V, \varphi \in H(U)$ such that

$$\begin{aligned} &(\mu^{-1} \, \mathbf{curl} \, \mathbf{a}, \mathbf{curl} \, \mathbf{a}') - \omega^2 (\epsilon \mathbf{a}, \mathbf{a}') + \\ &i\omega(\sigma \mathbf{a}, \mathbf{a}') + ((i\omega\epsilon + \sigma) \, \mathbf{grad} \, \varphi, \mathbf{a}') = (\mathbf{j}^s, \mathbf{a}'), \\ &(\epsilon \mathbf{a}, \mathbf{grad} \, \varphi') = 0 \end{aligned} \tag{13}$$

for all $\mathbf{a}' \in V, \varphi' \in H(0)$. $(\cdot, \cdot)$ denotes hereinafter the L^2 inner product

$$(f, g) = \int_V f g \, \mathrm{d}x.$$

$(\cdot, \cdot)_\Gamma$ denotes, correspondingly, the L^2 inner product with respect to the contact surface Γ as

$$(f, g)_\Gamma = \int_\Gamma f g \, \mathrm{d}x.$$

Further information can be found in [11].

3.1.4 Robust Formulation

It has been established that the formulation (13) is stable for high frequencies, but unstable for the stationary limit in non-conducting regions. Hence, a stabilized formulation is required. The instability arises when the scalar potential φ disappears in (13) for the stationary limit $\omega \to 0$ in non-conducting regions ($\sigma = 0$). In order to overcome this instability, a stabilized formulation introduced by [11] is employed in HADAPT.

The stabilization bases on φ being split into $\tilde{\varphi}$ and ψ in a non-conducting domain Ω_N. In order to balance the additional variable, Gauss' law is included in the Ω_N. This measure ensures that the potential no longer disappears from the equation for $\omega \to 0$. The details for this stabilization can be found in [11].

The resulting robust formulation can be expressed as

$$
\begin{aligned}
(\mu^{-1}\,\mathbf{curl}\,\mathbf{a}, \mathbf{curl}\,\mathbf{a}') - \omega^2(\epsilon\mathbf{a}, \mathbf{a}') + \\
i\omega(\sigma\mathbf{a}, \mathbf{a}') + ((i\omega\epsilon + \sigma)\,\mathbf{grad}\,\tilde{\varphi}, \mathbf{a}') = (\mathbf{j}^s, \mathbf{a}'), \\
(\epsilon\mathbf{a}, \mathbf{grad}\,\varphi') = 0, \\
(\epsilon\,\mathbf{grad}\,\tilde{\varphi}, \mathbf{grad}\,\psi') + (\epsilon\,\mathbf{grad}\,\psi, \mathbf{grad}\,\psi') = 0.
\end{aligned}
\tag{14}
$$

The system (14) is extended in the next section by deriving the contact resistance equation and subbing it into the system.

3.2 Contact Resistance Equation

The contact resistance equation is derived in this chapter. As the contact resistance is caused by the rough surfaces of a contact, these rough surfaces are modeled as one layer with thickness d and i reduced electric conductivities σ_i. The index i denotes the i-th a-spot. For an exact determination of σ_i, the knowledge of the a-spot distribution would be needed. As this thesis only is focused on a macroscopic simulation, a homogeneous a-spot distribution is assumed in the following. Accordingly, the electric conductivities σ_i are reduced to one uniform layer conductance σ_Γ. The layer, hereinafter, is denoted by $V_{adj,\Gamma}$ and shown in Figure 3 by the blue hatched area.

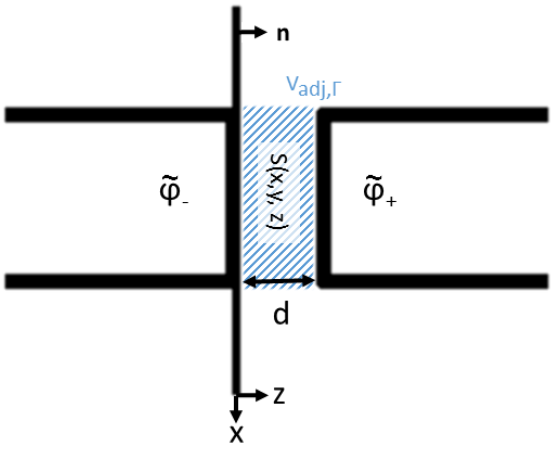

Figure 3: The contact resistance layer $V_{adj,\Gamma}$ is denoted by the blue hatched area and enclosed by two semi-infinite conductors.

Further, we assume that φ drops linearly in $V_{adj,\Gamma}$ due to its small thickness. The drops magnitude $s(x, y)$ is defined as the difference of the potentials $\tilde{\varphi}_+$ and $\tilde{\varphi}_-$, which are located at the boundaries of $V_{adj,\Gamma}$, i.e., $s(x, y) := \tilde{\varphi}_+ - \tilde{\varphi}_-$. Accordingly, the potential drop $s(x, y, z)$ can be expressed as a compact function

$$s(x,y,z) = \begin{cases} s(x,y) \cdot \frac{z}{d} & z \in \Omega_{V_{adj\Gamma}}, \\ 0 & \text{otherwise.} \end{cases} \tag{15}$$

$\Omega_{V_{adj,\Gamma}}$ denotes a domain comprising the volume adjacent to the contact surface Γ. (15) enforces the splitting of φ into $\bar{\varphi}$ and s such that $\tilde{\varphi} = \bar{\varphi} + s(x,y,z)$. $\bar{\varphi}$ denotes the continuous potential and $s(x,y,z)$ the potential drop due to the contact resistance.

As the solving of $s(x,y,z)$ is implemented on a mesh with a mesh size $h \gg d$, the mesh can not resolve the function $s(x,y,z)$. To overcome this, $s(x,y,z)$ is redefined into a discontinuous function. This discontinuous function can be expressed as

$$\lim_{z \to p} s(x,y,z) = \begin{cases} s(x,y) & p = -d, \\ 0 & p = +d, \\ 0 & otherwise. \end{cases}$$

Following the procedure in section 3.1.3, the contact resistance equation and its variational formulation are derived in the following paragraphs.

The electric field $\mathbf{e}_{V_{adj,\Gamma}}$ can be expressed as

$$\left.\begin{aligned} \mathbf{e}_{V_{adj,\Gamma}} &= -\,\mathbf{grad}\, s(x,y,z) \\ \Rightarrow \mathbf{e}_{V_{adj,\Gamma}} &= \frac{s(x,y)}{d} \cdot \mathbf{e}_z \end{aligned}\right\} \quad \text{in } \Omega_{V_{adj,\Gamma}}. \tag{16}$$

Possibly occurring inductive effects are assumed to be negligible due to the small conductivity between the conductor surfaces. Accordingly, the current density j_n in direction of the normal $\mathbf{n}$ can be expressed with the current density $\mathbf{j}_\Gamma = \sigma_\Gamma \mathbf{E}$ as

$$\begin{aligned} j_n &= \mathbf{j}_\Gamma \cdot \mathbf{n} \\ \Leftrightarrow j_n &= \sigma_\Gamma \mathbf{e}_{V_{adj,\Gamma}} \cdot \mathbf{n} \\ \overset{(16)}{\Rightarrow} j_n &= \sigma_\Gamma \frac{s(x,y)}{d} \cdot \mathbf{e}_z \cdot \mathbf{n} \\ \Leftrightarrow j_n &= \frac{\sigma_\Gamma}{d} s(x,y). \end{aligned} \tag{17}$$

Equation (17) can be derived in this way, as, due to the underlying physical problem, the current paths are restricted to paths through the a-spots, which are normal to the contact surface.

Also assuming that the charge accumulation can be neglected, the current is conserved with

$$\operatorname{div} \mathbf{j} = 0. \tag{18}$$

Multiplying (18) by a test function $s' \in H^1(\Omega_{V_{adj,\Gamma}})$ and integrating over $\Omega_{V_{adj,\Gamma}}$ results in the variational formulation

$$\int_{\Omega_{V_{adj,\Gamma}}} \operatorname{div} \mathbf{j} \cdot s' \, \mathrm{d}V = 0. \tag{19}$$

It is important to note that $\Omega_{V_{adj,\Gamma}}$ is limited to one arbitrarily chosen side of the contact, which is kept constant throughout the simulation. This yields the desired one sided drop in the potential. Integrating (19) by parts leads to the contact resistance equation

$$\begin{aligned}
\int_{\Omega_{V_{adj,\Gamma}}} \operatorname{div} \mathbf{j} \cdot s' \, \mathrm{d}V &= \int_{\Omega_{V_{adj,\Gamma}}} \mathbf{j} \cdot \mathbf{grad}\, s' \, \mathrm{d}V - \int_\Gamma j_n \cdot s' \, \mathrm{d}\Gamma = 0 \\
\Leftrightarrow \int_\Gamma j_n \cdot s' \, \mathrm{d}\Gamma &= \int_{\Omega_{V_{adj,\Gamma}}} \mathbf{j} \cdot \mathbf{grad}\, s' \, \mathrm{d}V \\
\overset{(17)}{\Rightarrow} \int_\Gamma \frac{\sigma_\Gamma}{d} s \cdot s' \, \mathrm{d}\Gamma &= \int_{\Omega_{V_{adj,\Gamma}}} -\sigma \cdot (\mathbf{grad}\, \tilde{\varphi} + i\omega \mathbf{A}) \cdot \mathbf{grad}\, s' \, \mathrm{d}V \\
\Leftrightarrow \int_\Gamma \frac{\sigma_\Gamma}{d} s \cdot s' \, \mathrm{d}\Gamma &= \int_{\Omega_{V_{adj,\Gamma}}} -\sigma \cdot (\mathbf{grad}(\bar{\varphi} + s) + i\omega \mathbf{A}) \cdot \mathbf{grad}\, s' \, \mathrm{d}V.
\end{aligned} \tag{20}$$

In the following the term σ_Γ / d is replaced by a measured or estimated contact resistance R_C, which is a required user input.

The below system of equations is derived by subbing (20) into (14) as additional equation. As before, $\tilde{\varphi}$ is split in (14) into $\bar{\varphi}$ and s. Hence, the implemented system can be expressed as

$$\begin{aligned}
(\mu^{-1} \mathbf{curl}\, \mathbf{a}, \mathbf{curl}\, \mathbf{a}') - \omega^2 (\epsilon \mathbf{a}, \mathbf{a}') + \\
i\omega(\sigma \mathbf{a}, \mathbf{a}') + ((i\omega\epsilon + \sigma)\, \mathbf{grad}(\bar{\varphi} + s), \mathbf{a}') &= (\mathbf{j}^s, \mathbf{a}'), \\
(\epsilon \mathbf{a}, \mathbf{grad}\, \varphi') &= 0, \\
(\epsilon\, \mathbf{grad}(\bar{\varphi} + s), \mathbf{grad}\, \psi') + (\epsilon\, \mathbf{grad}\, \psi, \mathbf{grad}\, \psi') &= 0, \\
(R_C s, s')_\Gamma + (\sigma \cdot (\mathbf{grad}(\bar{\varphi} + s) + i\omega \mathbf{A}), s') &= 0.
\end{aligned} \tag{21}$$

This system is implemented in the course of this thesis.

3.3 Finite Elements Method

The FEM can approximate solutions to boundary value problems for elliptic PDEs. In the FEM the solution space S is discretized into a finite space S_h. Further, the problem's domain is discretized into finite and simpler subdomains - the finite elements. For employing the FEM, the PDE

- is reformulated into a variational equation,
- a finite dimensional space S_h is chosen, and
- the problem is reformulated into a discrete problem yielding a system of equations.

In this thesis we apply the Ritz-Galerkin FEM to the contact resistance PDE. The Ritz-Galerkin FEM bases on the choice of the same subspace for the trial and test functions. The following brief introduction is based on [2], [4] and [9], where further information can be found.

The first step for applying the FEM is to reformulate the PDE into a variational formulation. This reformulation is already discussed in sections 3.1.3 and 3.2, and yields for our contact resistance PDE

$$(R_C s, s')_\Gamma + (\sigma \cdot (\mathbf{grad}(\bar{\varphi} + s) + i\omega\mathbf{A}), s') = 0.$$

After applying the variational formulation, Ritz-Galerkin approximates the solution s in the finite dimensional solution space S_h. This finite dimensional space $S_h(\Omega)$ is often defined as a subspace of the Sobolev space $H^1(\Omega)$. The h denotes the discretization into a finite dimensional space. For the sake of exemplariness, the Ritz-Galerkin method is in the following first applied to an example problem, extended to the FEM, and, at the end, applied to the contact resistance PDE. The example problem is the variational formulation of Poisson's equation: find $u \in H_0^1(\Omega)$ such that for all $u' \in H_0^1(\Omega)$

$$(\nabla u, \nabla u') = (f, u').$$

Replacing u by its approximate solution u_h, which is often referred to as trial function, yields

$$(\nabla u_h, \nabla u_h') = (f, u_h'). \tag{22}$$

u_h and the test function's approximation u_h' are now chosen to be in $S_h(\Omega)$, as required by the Ritz-Galerkin method.

The approximation's accuracy for u_h can be judged with the help of Cea's lemma.

Lemma 1 (Cea's lemma) *Let the bilinear form $a : H \times H \to \mathbb{R}$ be continuous and coercive. Then $u \in H$ and $u_h \in S_h$ of the continuous and discrete variational problems satisfy the relation*

$$\|u - u_h\|_H \leq \frac{C}{\gamma} \liminf_{v_h \in S_h} \|u - v_h\|_H.$$

Detailed information regarding the bilinear form and the coercive property including the lemma's proof can be found in [2]. Cea's lemma states that the solution's accuracy u_h is as precise as the approximation of u in S_h. This implies that the choice of S_h is essential for the solution's accuracy. Further it implies the validity of

$$\lim_{h \to 0} \|u - u_h\|_H = 0$$

for asymptotically dense subspaces S_h.

For letting the functions

$$\phi_j(x) = sin(j\pi x), \quad j = 1, ..., n$$

be basis functions in S_h, I choose the test function's approximation u'_h to be a linear combination of them. (22) changes for u'_h being replaced to

$$(\nabla u_h, icos(i\pi x) = (f, u'_{h_i}) \quad i = 1, 2, ..., n. \tag{23}$$

With the trial function u_h and u'_h chosen to be in the same space, u_h can be expressed by the same basis functions as

$$u_h = \sum_{k=1}^{n} u_k \phi_k(x),$$

where u_k denotes a constant factor corresponding to each basis function. Replacing u_h in (23) leads to

$$(\sum_{k=1}^{n} \nabla \phi_k(x) u_k, \nabla \phi_i(x)) = (f, \phi_i(x)) \quad i = 1, 2, ..., n.$$

As $(\cdot, \cdot)$ is linear, this can be simplified to

$$\sum_{k=1}^{n} [(\nabla\phi_k(x), \nabla\phi_i(x))u_k] = (f, \phi_i(x)) \quad i = 1, 2, ..., n. \tag{24}$$

The matrix formulation of (24) can be expressed as

$$Au = f,$$

with the matrix elements

$$a_{(i,k)} = (\nabla\phi_k(x), \nabla\phi_i(x)).$$

The FEM, in particular, is motivated by the pursuit of sparse matrices similar to matrices resulting from the finite differences. In order to achieve this, the domain is divided into a finite number of elements with polynomials defined on them. These polynomials are chosen to be in S_h. The domain's finite number of elements in combination with the polynomials are referred to as finite elements. Exemplary finite elements are tetrahedrons for three-dimensional domains. In order to ensure the sparseness, the polynomials are chosen to have a support, which is as small as possible. The term support denotes the set, for which the function is unequal to zero. It is differentiated between nodal based and edge based elements. The difference between both of them is that polynomials belonging to nodal based elements are defined for every node, whereas the polynomials belonging to edge based elements are defined for every edge.

In this thesis we used parabolic tetrahedrons which are defined by ten nodes; four main nodes at the corners and six auxiliary nodes on the edges. Parabolic tetrahedrons increase, in comparison to linear tetrahedrons, the accuracy of the approximation of u_h without changing the discretization mesh size h. In turn, this leads, according to Cea's Lemma, to a more precise approximation of the solution. An exemplary parabolic tetrahedron is shown in Figure 4 [7].

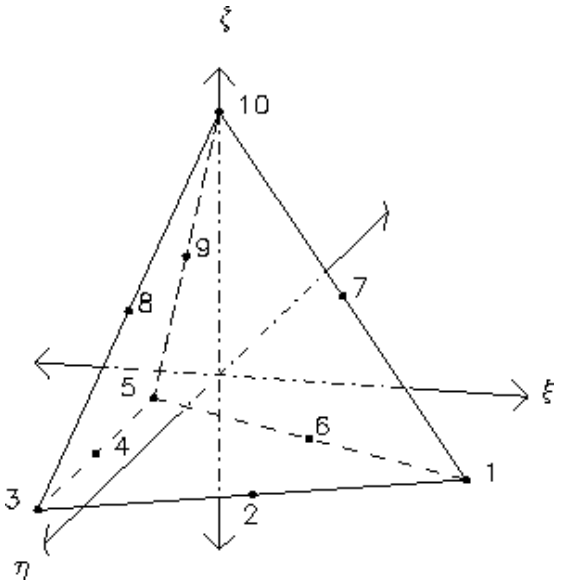

Figure 4: An exemplary parabolic tetrahedron.

For applying the FEM to the contact resistance PDE, the domains consisting of the device and the surrounding airbox are discretized. Therefor HADAPT is implemented to offer an interface to the commercial CAD tool Creo Parametric, which is used as a manual meshing tool. The resulting mesh is imported by HADAPT.

The scalar potential $\bar{\varphi}_h$ and the potential jump s_h use nodal based elements, whereas the discretized vector potential $\mathbf{a}_h$ uses edge based elements for their discretization. For N nodes in the domain Ω, N_V nodes in $\Omega_{V_{adj,\Gamma}}$ and E edges in Ω, the trial functions can be expressed as

$$\begin{aligned}
\varphi_h &= \sum_{i}^{N} \varphi_i \varphi_i', \\
s_h &= \sum_{m}^{N_V} s_m s_m', \\
a_h &= \sum_{k}^{E} a_k a_k',
\end{aligned}$$

with the element based polynomials chosen as

$$\begin{aligned}
\varphi_i', s_m' \quad &\in H_h^1, \\
a_k' \quad &\in \left\{ \mathbf{v} \in \mathbf{H}(\mathbf{curl}, \Omega) : \mathbf{curl}_\Gamma \, \mathbf{v_t} = 0 \, \text{on} \, \partial\Omega, \int_\tau \mathbf{v} \cdot \mathrm{d}s = 0 \right\}.
\end{aligned}$$

The test functions φ', s' and $\mathbf{a}'$ are chosen correspondingly as a linear combination of φ'_i, s'_m and $\mathbf{a}'_k$. Further information can be found in [15].

3.4 Thermal Model

The thermal simulation basing on the thermal model, calculates the temperature in the device and its environment. Therefore, the heat transfer through

- conduction,
- radiation,
- and convection

effects are simulated [5].

In the use case specified by ABB, the heat inside the device is distributed via heat conduction, whereas the thermal energy transfer between the device and the environment takes place by radiative and convective heat transfer. All heat transfer is solved inside the widely spread commercial computational fluid dynamics (CFD) solver Fluent. Further information is presented in section 4.0.3.

4 Solution Strategies for Linear Systems of Equations

This simulation consists of an electromagnetic simulation and a fluid dynamics simulation, which are solved separately. At first, the electromagnetic simulation is run by solving the system (21). After the simulation is finished, the resulting ohmic loss distribution is imported as energy source input into the CFD solver Fluent. By employing this input, Fluent computes the fluid dynamics simulation. The steps for solving the electromagnetic system are discussed in section 4.0.1, the interface between both solvers in section 4.0.2 and the fluid dynamics simulation in section 4.0.3.

4.0.1 Solving the System of Equations

The implemented electromagnetic system is expressed in (21). This system is sparse due to the local support property of finite element test functions. As direct methods fill the matrix usually with additional non-zero elements during the elimination steps, they are only suitable for small systems. Therefore, the iterative method BiCGStab, a Krylov subspace method, is used in HADAPT.

Krylov subspace methods are common solving methods for sparse linear system of equations. They are based on projection processes onto the Krylov subspaces K_m. The subspace K_m of step m is spanned by a $n * n$- matrix A and a n-vector b as

$$K_m = span\{b, Ab, A^2b, .., A^{m-1}b\}.$$

Widely spread Krylov subspace methods are e.g., the CG-method, MINRES and BiCGStab, which can be found in detail in [4] and [20]. The preconditioned version of the BiCGStab method, a stabilized and optimized version of the CG-method, is used for solving this system. A preconditioner can improve the convergence speed, as it changes the system's set of eigenvalues. A new set of eigenvalues may lead to less required iterative steps and, therefore, the iterative method may converges faster. The preconditioned equation can be expressed as

$$P^{-1}Ax = P^{-1}b,$$

which is equivalent to the initial equation

$$Ax = b.$$

In HADAPT two preconditioners are implemented and chosen based on the system's size; one basing on a LU decomposition by PARDISO and one basing on the operator preconditioning theory. For rather small simulations with up to $250\,000$ elements, the preconditioner based on the LU decomposition is employed and computed by PARDISO [21]. For bigger simulations with more than $250\,000$ elements, the operator preconditioning following [10] is applied. Both preconditioners, their derivation, and application to contact resistances are discussed in the next paragraphs.

The LU decomposition solves regular linear systems of equations directly. As the splitting of $\tilde{\varphi}$ in section 3.1.4 leads to the system (21) being singular, it can not be solved by the LU decomposition [15]. To overcome this, the lower bounds

$$\begin{aligned} \omega &= max\{\omega, 1\,\mathrm{Hz}\}, \\ \sigma(x) &= max\{\sigma(x), 1\,\frac{\Omega}{\mathrm{m}}\}, \end{aligned}$$

are imposed for the system yielding a new regular system. The bounds are applied to the new equation as well. For this new regular system, the LU decomposition is computed by a shared-memory multiprocessing parallel direct sparse solver contained in Intel's MKL. Detailed information regarding the solver, PARDISO, can be found in [14]. The solution of the new system is employed as start guess for the BiCGStab method along with a basic preconditioner. This improves the convergence to maximal 5 iterative steps [15].

As the LU decomposition can only be applied to small systems, a more efficient preconditioner is applied to bigger systems. The employed preconditioner is based on the operator preconditioning, whose theory can be found in [18] and [10]. The existing HADAPT preconditioner framework

$$\mathbf{P}\begin{pmatrix} \mathbf{A} \\ \tilde{\varphi} \\ \psi \end{pmatrix} := \begin{pmatrix} \mathbf{curl}\,\frac{1}{\mu}\,\mathbf{curl}\,\mathbf{A} + \omega\sigma\mathbf{A} & 0 & 0 \\ 0 & \operatorname{div}\epsilon\,\mathbf{grad}\,\tilde{\varphi} & 0 \\ 0 & 0 & \operatorname{div}\epsilon\,\mathbf{grad}\,\psi \end{pmatrix},$$

is extended in order to apply it to the system (21). The extended preconditioner can be expressed as

$$\mathbf{P}\begin{pmatrix}\mathbf{A}\\ \tilde{\varphi}\\ \psi\\ s\end{pmatrix} := \begin{pmatrix}\mathbf{curl}\,\frac{1}{\mu}\,\mathbf{curl}\,\mathbf{A}+\omega\sigma\mathbf{A} & 0 & 0 & 0\\ 0 & \operatorname{div}\epsilon\,\mathbf{grad}\,\tilde{\varphi} & 0 & 0\\ 0 & 0 & \operatorname{div}\epsilon\,\mathbf{grad}\,\psi & 0\\ 0 & 0 & 0 & R_C s+\sigma\,\mathbf{grad}\,s\end{pmatrix} \quad (25)$$

Unfortunately, (25) has proven not to be effective for some systems and, on average, leads to a convergence after 25-40 steps. Hence, further investigation in a more effective preconditioner is planned with the alternative preconditioner

$$\mathbf{P}\begin{pmatrix}\mathbf{A}\\ (\tilde{\varphi}\quad s)\\ \psi\end{pmatrix} := \begin{pmatrix}\mathbf{curl}\,\frac{1}{\mu}\,\mathbf{curl}\,\mathbf{A}+\omega\sigma\mathbf{A} & 0 & 0\\ 0 & (\operatorname{div}\epsilon\,\mathbf{grad}\,\tilde{\varphi} & R_C s+\sigma\,\mathbf{grad}(\bar{\varphi}+s)) & 0\\ 0 & 0 & \operatorname{div}\epsilon\,\mathbf{grad}\,\psi\end{pmatrix}.$$

4.0.2 Coupling Electromagnetic - Fluid Dynamics

The coupling between the electromagnetic solver HADAPT and the CFD solver Fluent is presented in this section. As the electromagnetic simulation is run at first, the resulting ohmic losses need to be transferred to Fluent. These losses are exchanged by using a file interface. These files contain the elements center coordinates, their radii, volume, and power loss density in $\frac{\mathrm{W}}{\mathrm{m}^3}$. Fluent and HADAPT use different meshes and, thus, these data have to be mapped and scaled by Fluent. The usage of different meshes results from the different requirements of the simulations; the fluid simulation requires a fine discretization of the fluid close to the wall, whereas the electromagnetic simulation requires a fine discretization inside the conductors. In oder to optimize the simulation's results and minimize the system's size, different meshes are employed.

The mapping needs to map the ohmic losses from a tetrahedral mesh to either a tetrahedral or a hexahedral mesh of arbitrary discretization size. An exemplary mapping configuration is shown with superposed meshes [17] in Figure 5.

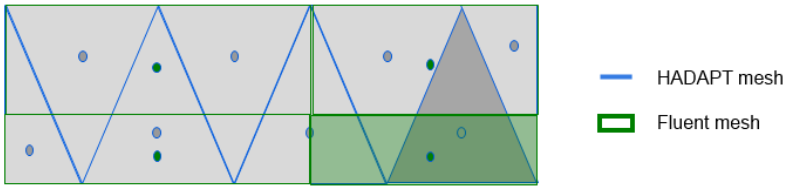

Figure 5: A HADAPT mesh superposed with a Fluent mesh and the elements' center denoted by the colored dots.

For mapping the ohmic losses calculated for the HADAPT mesh precise and efficient, they are distributed according to the elements' intersecting volumes. This is calculated by

$$loss_{Fluent-i} = \frac{\sum_k loss_{HADAPT_k} \cdot (V_{Fluent-i} \cap V_{HADAPT-k})}{\sum_k (V_{Fluent-i} \cap V_{HADAPT-k})}.$$

4.0.3 Computational Fluid Dynamics

The CFD simulation comprises the conduction, radiation and convection effects mentioned in section 3.4. For the simulation to be set up and started correctly, a journal file, which automates the execution of Fluent, is provided along with HADAPT. It sets basic physical and numerical settings as well as the boundary conditions. The mapped loss density is hereby taken as energy source input. The employed physical models include the SST - k ω model, a pressure based first-order solver and the s2s radiation model. Further information regarding these models can be found in [1].

5 Evaluation

In this chapter we evaluate the implemented electro-thermal simulation of contact resistances in order to show its validity and ability to comply with some basic electric laws. For being valid, the impact of contact resistances needs to equal the impact of infinitesimal small volume resistances. This is validated in section 5.1.1 by examining the global convergence between an arbitrarily chosen contact resistance and a volume resistance of varying thickness d. The term global convergence denotes hereinafter the convergence of the difference between the time averaged power losses of the volume resistance domain and the contact resistance domain. Further, a simulation of a circuit with two parallel contact resistances needs to obey Kirchhoff's law, which is verified in section 5.1.2. This is followed in section 5.1.3 by validating the simulation of a contact resistance in the limit $\sigma_c \to \inf \frac{\mathrm{S}}{\mathrm{m}}$, i.e., examining the simulation's behavior for a contact resistance C with $C \to 0\,\Omega$. For a combined electro - thermal simulation, the feasibility is shown in section 5.2 for an exemplary ABB business unit device.

5.1 Electromagnetic Simulation

5.1.1 Global Convergence

In this section the convergence of volume resistances with infinitesimal small thickness d to a contact resistance is examined. For this purpose, a circuit comprising a volume resistance and a circuit comprising a contact resistance are simulated. They are hereinafter referred to as volume circuit and contact circuit, respectively. The volume circuit is shown in Figure 6 and comprises two copper conductors of fixed length $5\,\mathrm{cm}$ with the conductivity σ_{Cu}. These conductors enclose a volume resistance, whose thickness d and conductivity σ_R varies throughout the simulation runs. This circuit is excited by a voltage load of $10\,V$ at the frequencies $f = 0\ \mathrm{sec}^{-1}$ and $f = 50\ \mathrm{sec}^{-1}$. In the course of this study, the total resistance of the volume circuit R_{total} is kept constant at $R_{total} = 5.1946 \times 10^{-5}\,\Omega$ by varying σ_R according d. The corresponding values for d and σ_R are listed in Table 1.

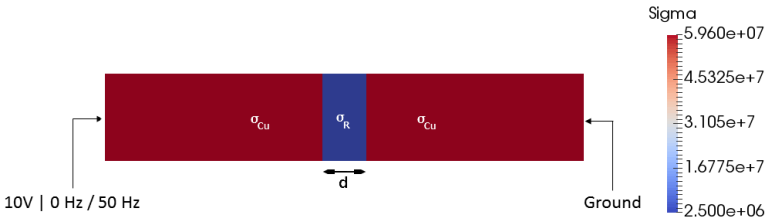

Figure 6: The volume circuit with $d = 1\,\mathrm{cm}$ and $\sigma_R = 2.5 \times 10^6\,\mathrm{S/m}$. The colors illustrate the conductivity sigma in $\mathrm{S/m}$.

The contact circuit is shown in Figure 7. In comparison to the volume circuit, the volume resistance is replaced by a contact resistance C with the restistance $C = 1 \times 10^{-5}\,\Omega$. The copper conductors and the excitation are kept equal.

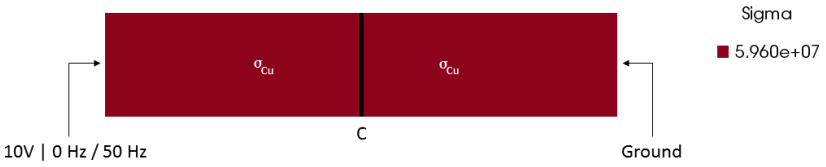

Figure 7: The contact circuit $C = 1 \times 10^{-5}\,\Omega$. The colors illustrate the conductivity sigma in $\mathrm{S/m}$.

$d\,[\mathrm{cm}]$	$\sigma_R\,[\mathrm{S/m}]$
1	2.5×10^6
0.5	1.25×10^6
0.25	6.25×10^5
0.125	3.125×10^5
0.0625	1.5625×10^5
0.03125	$0.781\,25 \times 10^5$

Table 1: Volume domain's conductivity values for the varying d

The simulation of the volume circuit is run for each pair of values in Table 1. This yields the time averaged ohmic power losses of the volume resistance domain, which are listed in Table 2. The simulation of the contact circuit is run only once with the contact resistance $C = 1 \times 10^{-5}\,\Omega$ yielding the time averaged ohmic power loss of the contact resistance domain as $P_{avg} = 4.96 \times 10^6\,\mathrm{W}$ for $0\,\mathrm{Hz}$ and $P_{avg} = 1.65 \times 10^6\,\mathrm{W}$ for $50\,\mathrm{Hz}$. These results are now evaluated by calculating the absolute and relative difference between the results of the contact resistance domain and of the volume resistance domain stated above and in Table 2.

	$P_{avg}\,[\mathrm{W}]$	
$d\,[\mathrm{cm}]$	$0\,\mathrm{Hz}$	$50\,\mathrm{Hz}$
1	4.96×10^6	1.55×10^6
0.5	4.96×10^6	1.60×10^6
0.25	4.96×10^6	1.62×10^6
0.125	4.96×10^6	1.64×10^6
0.0625	4.96×10^6	1.64×10^6
0.03125	4.96×10^6	1.65×10^6

Table 2: The time averaged power losses of the volume resistance domain for every d

The expected result for the simulation is that the absolute and relative differences approach 0 for $d \to 0$.

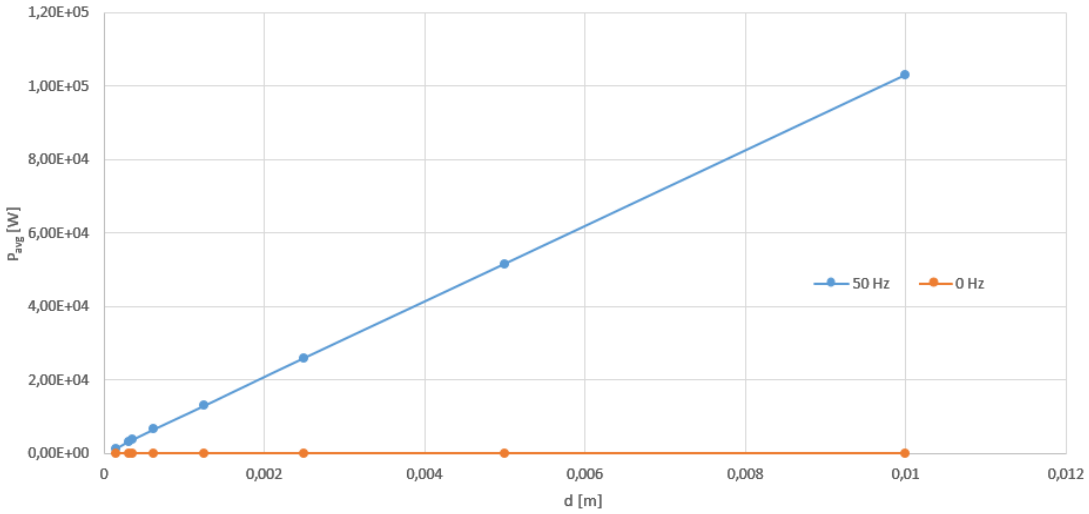

Figure 8: The absolute difference between the contact resistance domain's and volume resistance domains' time averaged ohmic power losses for varying thicknesses d.

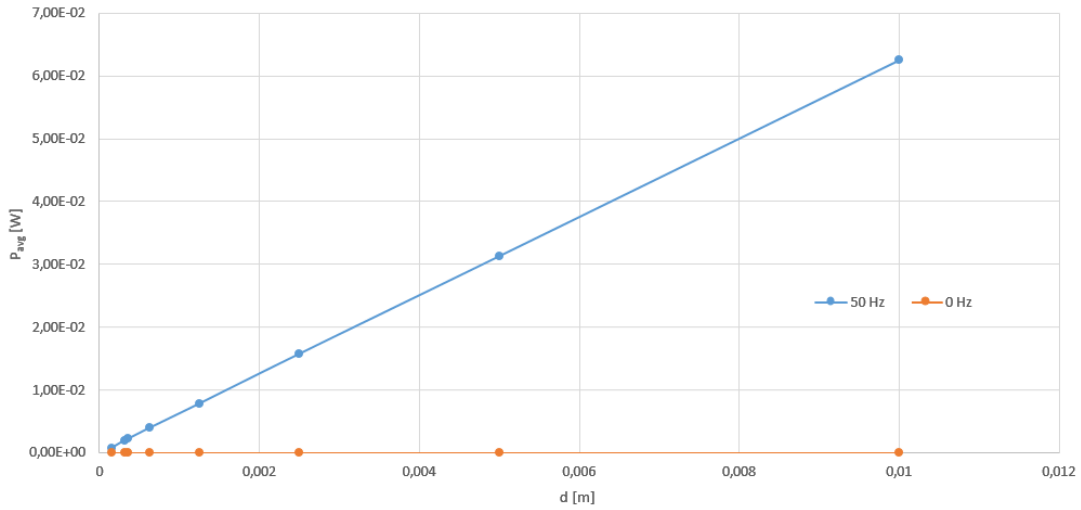

Figure 9: The relative difference between the contact resistance domain's and volume resistance domains' time averaged ohmic power losses for varying thicknesses d.

For $0\,\mathrm{Hz}$, Figures 8 and 9 show that the difference between the time averaged ohmic power losses of the two resistance domains are equal 0 for every d. The behavior differs, however, at $50\,\mathrm{Hz}$. In this case, there is a relative difference of 0.06 for $d = 1\,\mathrm{cm}$. This difference decreases linearly from 0.06 to 0 at the extrapolated intersection with the x-axis. The intersection is at the point $0, 0$, which implies that the relative difference approaches 0 for d approaching 0. This shows that volume resistances converge to contact resistances globally for $d \to 0$.

5.1.2 Kirchhoff's Law

Kirchhoff's law allows basic circuit calculation based on the conservative property of the electric field [24]. It states that the sum of all elements' voltage drops U_i in a closed loop equals zero. For this verification, the circuit shown in Figure 10 is used, which consists of two contact resistances C_1 and C_2. Their values for the two simulation runs are listed in Table 3.

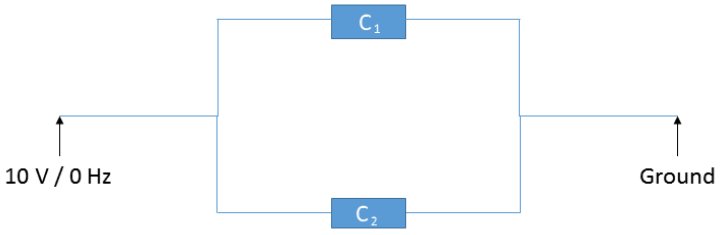

Figure 10: Schematic drawing of the circuit used in the following simulations.

	C_1	C_2
Simulation 1	$1 \times 10^{-3}\,\Omega$	$1 \times 10^{-3}\,\Omega$
Simulation 2	$1 \times 10^{-3}\,\Omega$	$2 \times 10^{-3}\,\Omega$

Table 3: The resistance values in Ω

Important to note is that a conductivity σ_{high}, whose value is much larger than the conductivity of copper, is assigned to the wires. This enables us to neglect the wire resistance in the following calculations.

In the first simulation run, both contact resistances are assigned with a resistance value of $1 \times 10^{-3}\,\Omega$, i.e., $C_1 = C_2 = 1 \times 10^{-3}\,\Omega$. By using Kirchhoff's and Ohm's law, the resulting currents I_1 and I_2 are calculated as

$$\begin{aligned} U_{C1} - U_{C2} &= 0, \\ \Leftrightarrow C_1 I_1 - C_2 I_2 &= 0, \\ \Rightarrow I_1 &= I_2. \end{aligned} \tag{26}$$

This predicts the equality of the currents through the contacts. For evaluating this prediction, the current density distribution, which is shown in Figure 11, is integrated over the contact areas Γ_{c_1} and Γ_{c_2}. The results are listed in Table 4 and comply with the prediction stated in (26).

	C_1	C_2
I [A]	249.998	249.998

Table 4: Resulting currents at C_1 and C_2

A further implication of the prediction in this case is a symmetry of the current density distribution with respect to a horizontal axis. This symmetry can be seen in Figure 11.

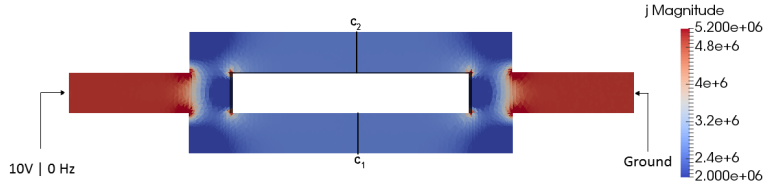

Figure 11: The current density distribution for two parallel equal contact resistances.

In the second simulation run, the contact resistances are assigned with the resistance values $2C_1 = C_2 = 2 \times 10^{-3}\,\Omega$. The currents I_1 and I_2 are predicted by Kirchhoff's law as

$$\begin{aligned} U_{C1} - U_{C2} &= 0 \\ \Leftrightarrow C_1 I_1 - C_2 I_2 &= 0 \\ \Rightarrow I_1 &= 2\frac{C_2}{C_2} I_2 \\ I_1 &= 2I_2. \end{aligned} \tag{27}$$

This implies that the current I_1 flowing through C_1 is double the size of the current I_2 flowing through C_2. This is evaluated by integrating the current density distribution over the contact surfaces Γ_{C_1} and Γ_{C_2}. The currents result as $I_1 = 499,993\,\mathrm{A}$ and $I_2 = 249,997\,\mathrm{A}$. The resulting ratio of $1,999996$ complies with the prediction in (27). The occurring inaccuracy is due to the neglect of the wire resistances and their voltage drops.

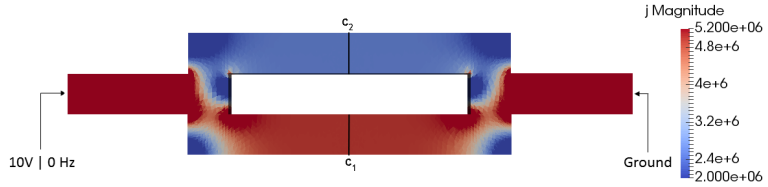

Figure 12: The current density distribution for two parallel unequal contact resistances.

Hence, the validity of Kirchhoff's law is shown for both simulations.

5.1.3 Vanishing Contact

A contact resistance in the limit $C \to 0$ is simulated in this section. The expected result is that the impact on the current flow vanishes. The current flow in AC circuits is dominated by the skin effect, which leads to a higher current density at the boundary of the conductor. The corresponding characteristic skin depth δ is determined by

$$\delta = \sqrt{\frac{2\rho}{\omega\mu}} \sqrt{\sqrt{1 + (\rho\omega\epsilon)^2} + \rho\omega\epsilon}.$$

From this formula, it can be derived that with rising resistivity ρ, the skin effect is attenuated, i.e., δ becomes larger. Therefore, showing the lack of this atten-

uation verifies that the contact resistance vanishes in the limit $C \to 0\,\Omega$. This verification is done graphically by examining the skin depths and comparing to a simulation without a contact resistance for several simulation runs.

The circuit shown in Figure 7 is used in the simulation. Its contact resistance C changes for the different simulation runs to the values listed in Table 5. During the simulation, the circuit is excited by a voltage load of $10\,\mathrm{V}$ at $50\,\mathrm{Hz}$.

	R_C
Simulation 1	$2.5 \times 10^{-8}\,\Omega$
Simulation 2	$2.5 \times 10^{-10}\,\Omega$
Simulation 3	$2.5 \times 10^{-12}\,\Omega$

Table 5: Resistance values in the limit to 0

The simulations yield the following current density distributions for the decreasing contact resistance C.

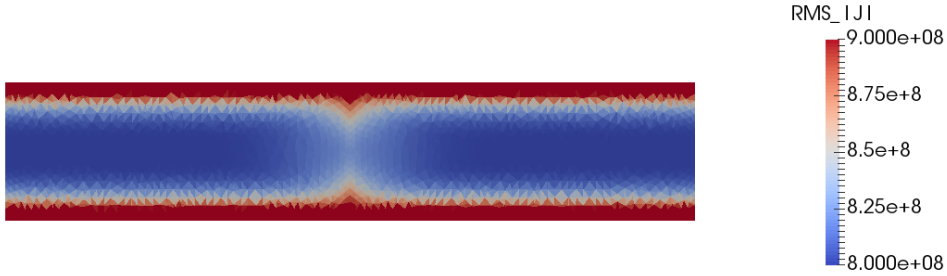

Figure 13: The current density distribution for $C = 2.5 \times 10^{-8}\,\Omega$.

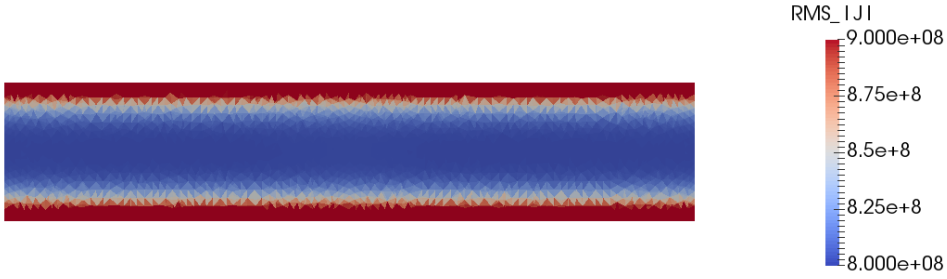

Figure 14: The current density distribution for $C = 2.5 \times 10^{-10}\,\Omega$.

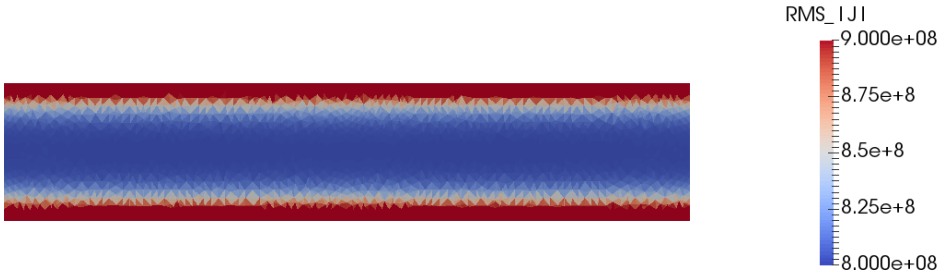

Figure 15: The current density distribution for $C = 2.5 \times 10^{-12}\,\Omega$.

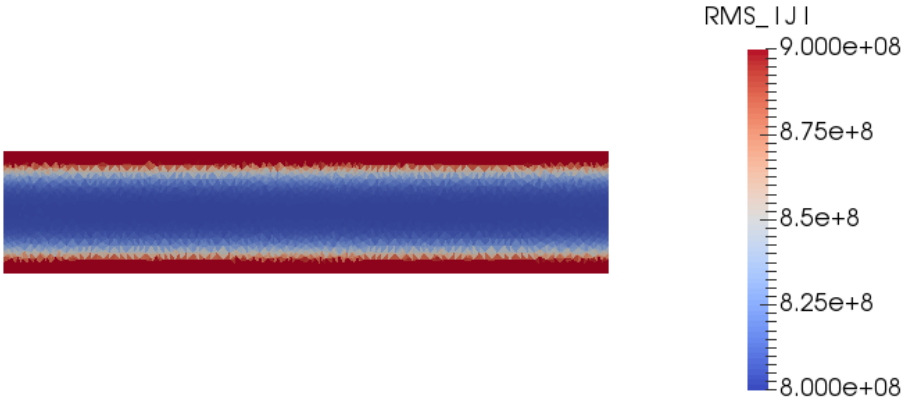

Figure 16: The current density distribution for $C = 0$.

For $C = 2.5 \times 10^{-8}\,\Omega$ the skin effect and its attenuation can clearly be seen in Figure 13. This becomes visible through a change in the skin depth, which is width of the region with high current density located at the conductor boundaries. In contrast, for $C = 2.5 \times 10^{-10}\,\Omega$ and smaller, no change in the skin depth can be seen in Figures 14 and 15. This implies that a contact resistance of less than $2.5 \times 10^{-10}\,\Omega$ does not have a visible impact on the circuit in terms of an additional resistance.

Comparing the current density distribution of the circuit shown in 16 to the circuits in Figures 14 and 15, shows no difference in the current distribution or magnitude. Hence, the simulation of vanishing contact resistances in the limit $C \to 0$ complies with simulations without a contact resistance.

5.2 Thermal Simulation

The thermal simulation yields the heat distribution in the system. Therefore, the losses are mapped to the Fluent mesh and taken as energy source, as described in section 4.0.2. Fluent is set to solve the energy, turbulent flow and

radiation equations up to the steady state. In this section the feasibility of thermal simulations for contact resistances is shown exemplarily for an ABB business unit example, whose optimization is a current subject of research.

The contact finger was provided as a computer-aided design (CAD) file and is shown in Figures 17 and 18. It consists of an aluminum block, a copper contact finger, and a copper conductor, which are denoted by bright silver, the red and green, and the yellow parts, respectively. The contact finger is connected to a $200\,\mathrm{A}$ DC power source by the cable on both sides. The contact finger's length is $177\,\mathrm{mm}$.

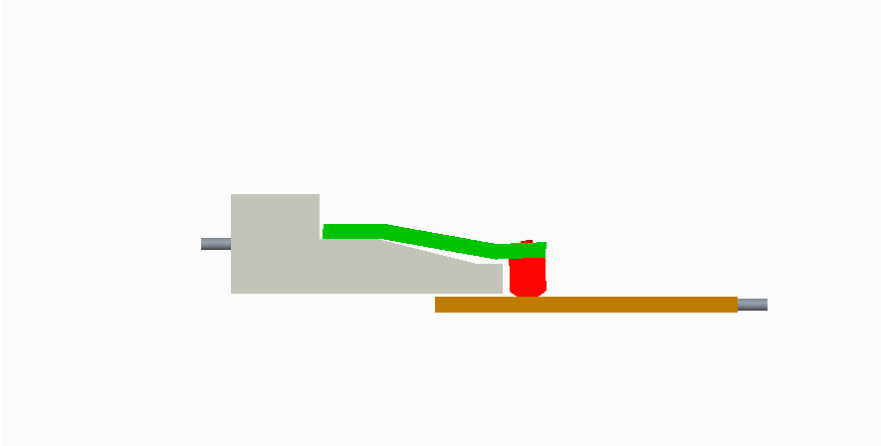

Figure 17: Front view of the contact finger, which is used for the simulation. The colors only denote different parts.

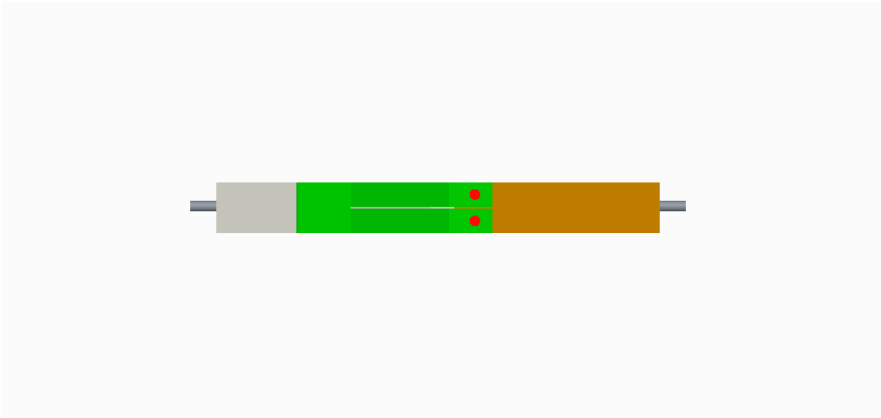

Figure 18: Top view of the contact finger, which is used for the simulation. The colors only denote different parts.

The electromagnetic simulation is run with a current excitation of $200\,\mathrm{A}$ at $0\,\mathrm{Hz}$. For the thermal simulation we surrounded the contact finger by a box filled with air at atmospheric pressure. Its boundary conditions are set to a temperature boundary condition with a constant value of $24.9°\mathrm{C}$. Between the solids

and the air convection and radiation boundary conditions are set. In order to visualize the heating resulting from the contact resistance and the contact finger's resistivity, the heat flux at the cable boundaries is set to 0. The results are visualized in Figures 19 and 20 and show the feasibility of the electro thermal simulation.

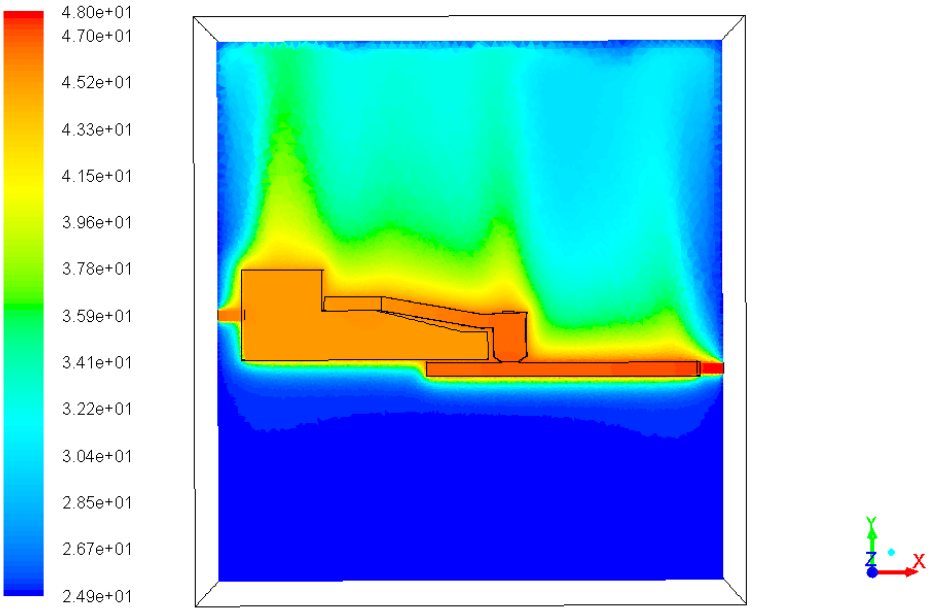

Figure 19: A front view of the contact finger, which is used for the simulation. The colors denote the temperature in $°C$.

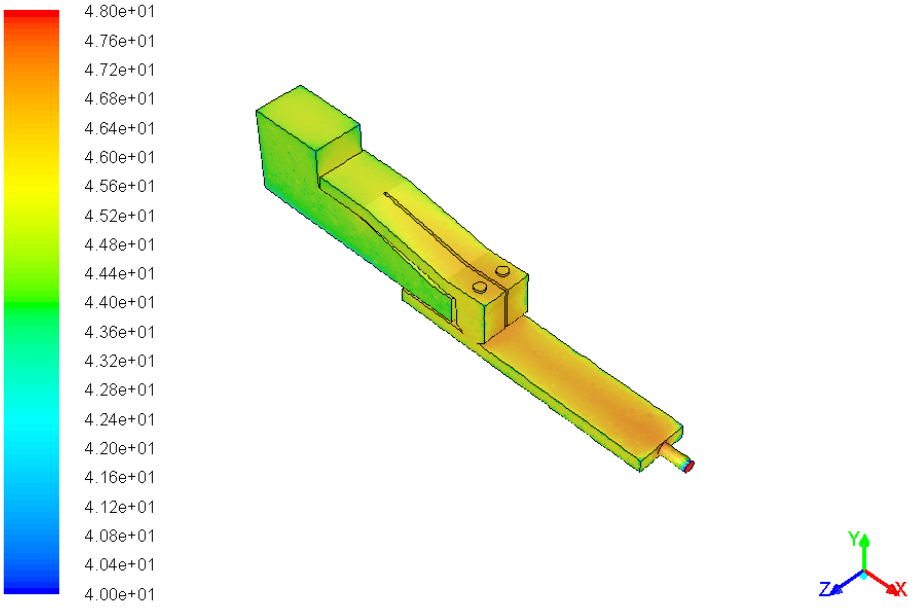

Figure 20: An isometric view of the contact finger, which is used for the simulation. The colors denote the temperature in $°C$.

6 Outlook

The capability of HADAPT to simulate devices comprising contact resistances arise a lot of new use cases. Power devices with arbitrary configurations can now be simulated with respect to the occuring contact resistances. As the simulation, implemented in the course of this thesis, is neglecting the possibly varying influences on the contact resistance, it needs to be extended. These influences can, for example, change the contact resistance due to mechanical forces or high temperatures. Moreover, further electromagnetic effects occur in electronic contacts such as the Holm forces, which can lead to a temporary disconnection of the contact and therefore to an arc.

This shows, that in order to optimize the outcome of the simulations, these impacts have to be included into HADAPT. Therefore, some necessary extensions are listed below.

- The macroscopic simulation has to be coupled with a mechanic solver, which yields the surface changes due to arising forces.
- The resistivities have to change according to their temperature dependence.
- The losses transfer and the iteration between Fluent and HADAPT should be automatized in order to increase the user-friendliness.
- As mentioned in chapter 4, the iterative preconditioner has to be optimized for increasing the simulation speed.

References

[1] ANSYS. Ansys fluent theory guide.

[2] Braess, D. (2007). *Finite Elemente*, Volume 52. Spektrum Akademischer Verlag Heidelberg.

[3] Braunovic, M., V. V. Kochnits, and N. K. Myshkin (2006). *Electrical Contacts: Fundamentals, Applications and Technology*. CRC Press.

[4] Dahmen, W. and A. Reusken (2008). *Numerik für Ingenieure und Naturwissenschaftler*. Springer Berlin Heidelberg.

[5] Faghri, A., Y. Zhang, and J. R. Howell (2010). *Advanced Heat and Mass Transfer*. Global Digital Press.

[6] Felsen, L. B. and M. Mongiardo (2009). *Electromagnetic Field Computation by Network Methods*. Springer-Verlag.

[7] Greenough, C. (2000). TET10 - Finite Element Library Shape Function.

[8] Greenwood, J. A. (2002). Constriction resistance and the real area of contact. *British Journal of Applied Physics 17*(12), 1621–1632.

[9] Hiptmair, R. (2002). Finite elements in computational electromagnetism. *Acta Numerica 1*, 237–339.

[10] Hiptmair, R. (2006). Operator Preconditioning. *Computers and Mathematics with Application 52*, 699–706.

[11] Hiptmair, R., F. Krämer, and J. Ostrowski (2008). A robust Maxwell formulation for all frequencies. *IEEE Transactions on Magnetics 44*(6), 682–685.

[12] Holm, R. (1958). *Electrical Contacts Handbook*, Volume 19. Springer-Verlag.

[13] Holm, R. and W. Meissner (1932). Kontaktwiderstand zwischen Supraleitern und Nicht-supraleitern. Messungen mit Hilfe von flüssigem Helium. *Zeitschrift für Physik 74*, 715–735.

[14] Intel. Intel MKL PARDISO - Parallel Direct Sparse Solver Interface.

[15] Krämer, F. (2008). *Schnelle und stabile Behandlung der Maxwell-Gleichungen im stationären Fall*. Diplomarbeit, Universität zu Leipzig.

[16] Nolting, W. (2001). *Grundkurs Theoretische Physik 3*. Springer Berlin Heidelberg.

[17] Ostrowski, J. M. Electro-Thermal Simulations. Technical report, ABB.

[18] Ostrowski, J. M., M. Bebendorf, R. Hiptmair, and F. Krämer (2010). H-Matrix-Based Operator Preconditioning for Full Maxwell at Low Frequencies. *IEEE TRANSACTIONS ON MAGNETICS 46*(8).

[19] Quarteroni, A. and A. Valli (2008). *Numerical Approximation of Partial Differential Equations*. Springer Berlin Heidelberg.

[20] Saad, Y. (2003). *Iterative Methods for Sparse Linear Systems* (2nd ed.). SIAM.

[21] Schenk, O. (2007). PARDISO Project.

[22] Timsit, R. S. (1977). The potential distribution in a constricted cylinder. *Journal of Physics D: Applied Physics 10*(15), 2011–2017.

[23] Timsit, R. S. (1999). Electrical contact resistance: properties of stationary interfaces. *IEEE Transactions on Components and Packaging Technologies 22*(1), 85–98.

[24] Tipler, P. A. and G. Mosca (2007). *Physik: für Wissenschaftler und Ingenieure*. Spektrum Akademischer Verlag Heidelberg.

Eidesstattliche Versicherung

Name, Vorname

Matrikelnummer (freiwillige Angabe)

Ich versichere hiermit an Eides Statt, dass ich die vorliegende Arbeit/Bachelorarbeit/ Masterarbeit* mit dem Titel

selbständig und ohne unzulässige fremde Hilfe erbracht habe. Ich habe keine anderen als die angegebenen Quellen und Hilfsmittel benutzt. Für den Fall, dass die Arbeit zusätzlich auf einem Datenträger eingereicht wird, erkläre ich, dass die schriftliche und die elektronische Form vollständig übereinstimmen. Die Arbeit hat in gleicher oder ähnlicher Form noch keiner Prüfungsbehörde vorgelegen.

Ort, Datum

Unterschrift

*Nichtzutreffendes bitte streichen

Belehrung:

§ 156 StGB: Falsche Versicherung an Eides Statt

Wer vor einer zur Abnahme einer Versicherung an Eides Statt zuständigen Behörde eine solche Versicherung falsch abgibt oder unter Berufung auf eine solche Versicherung falsch aussagt, wird mit Freiheitsstrafe bis zu drei Jahren oder mit Geldstrafe bestraft.

§ 161 StGB: Fahrlässiger Falscheid; fahrlässige falsche Versicherung an Eides Statt

(1) Wenn eine der in den §§ 154 bis 156 bezeichneten Handlungen aus Fahrlässigkeit begangen worden ist, so tritt Freiheitsstrafe bis zu einem Jahr oder Geldstrafe ein.

(2) Straflosigkeit tritt ein, wenn der Täter die falsche Angabe rechtzeitig berichtigt. Die Vorschriften des § 158 Abs. 2 und 3 gelten entsprechend.

Die vorstehende Belehrung habe ich zur Kenntnis genommen:

Ort, Datum

Unterschrift